MSDE

ROYAL SOCIETY OF CHEMISTRY

MINI REVIEW

View Article Online
View Journal | View Issue

Check for updates

Cite this: *Mol. Syst. Des. Eng.*, 2022, 7, 553

Received 28th January 2022,
Accepted 4th April 2022

DOI: 10.1039/d2me00020b

rsc.li/molecular-engineering

Advances in morphology control of organic semiconductor enabled organic transistor-based chemical sensors

Danfeng Zhi, Enyu Zhang, Boya Zhang and Fengjiao Zhang *

Electronic sensors have achieved tremendous progress in research and industry fields, and organic transistors are being developed as potential candidates with high performance and low cost. Considering the carrier transport and signal transition occurring within the active layer in the transistor, controlling the molecular stacking and microstructure of organic semiconductor films becomes an attractive alternative for achieving high sensitivity and selectivity. In this review, we provide a brief overview of the fundamentals of organic transistor based chemical sensors, as well as the advantages and the mechanisms of morphology dependent sensing performance in organic transistors. In addition, we give an insight into the strategies developed to manipulate the film properties in chemical sensors. Further, we also discuss current challenges and opportunities in the morphology control of organic transistor-based sensors toward practical applications.

Design, System, Application

Organic transistors have attracted increasing interest in flexible electronics due to their high performance, low-cost fabrication, outstanding flexibility and good biocompatibility. In the past decades, organic transistors, with the capability of intrinsic signal transformation and amplification, have emerged as one of the promising chemical sensing platforms in health monitoring and environmental detection. Benefiting from the rapid development of materials sciences and construction techniques, there are several excellent reviews for enhanced chemical detection reported from the perspectives of molecular design, interface engineering, and device integration. Recently, many studies have proved that the multiscale morphology of the organic semiconductor layer plays a critical role in the sensing performance, by controlling the carrier transport properties and interactions between the conductive channel and analytes. Hence further improvement of the sensing performance of organic transistor-based chemical sensors requires a better understanding of the relationship among the molecular packing, microstructure, and device performance. Here, we briefly summarize the mechanisms of film morphology enabled chemical detection, and the strategies for multiscale morphology control. This review is likely to be of interest to university researchers, engineers and graduate students in materials science and electronics who are working on the functional application of organic transistors.

1 Introduction

Sensors with wide applications in various research fields are attracting increasing interest in both academia and industry. The sensitive and selective detection of chemical species in both the human body and the surrounding environment, in a noninvasive and inexpensive way, is an appealing solution for environmental and health issues. An electrical sensor supports general signal recognition methods with a simple device configuration and detection equipment. Organic transistors, which are three-terminal devices with electrical-signal-transduction functionality, have been proposed as promising candidates for chemical and biological monitoring because of their specific features of outstanding flexibility, good compatibility and low cost.[1–4] The molecular tailorability and easy processability of organic semiconductors (OSCs) have led to the extensive development of organic transistors for high-throughput and large-scale integrated devices for personalized healthcare.[5,6] More importantly, organic transistors can exhibit excellent signal transduction and amplification with low power consumption,[2,7,8] making them platforms for wearable electronics and the internet of things.

To date, three types of organic transistors have been applied to chemical/biosensors: conventional organic field-effect transistors (OFETs), electrolyte-gated OFETs (EGOFETs) and organic electrochemical transistors (OECTs). When the devices are exposed to chemical stimuli, the analytes interact with the active layer *via* doping, quenching and dipole effects,[8,9] causing changes in the carrier concentration and/or carrier transport. As the active layer component, OSCs play a critical role in electronic sensors because carrier accumulation and transport mainly occur in the conductive

---

School of Chemical Sciences, University of Chinese Academy of Sciences, Beijing 100049, China. E-mail: fjiaozhang@ucas.ac.cn

channel. Hence, the electronic and sensing properties are highly dependent on the molecular structure and multiscale morphology because of the following factors: 1) the transconductance, which reflects the amplification functionality, depends on the delocalization of π-electrons along the interchain and intrachain, 2) the charge transfer between the carriers in the conductivity channel and analytes, and 3) the effective reaction sites provided by the contact interfaces to the analyte species. Notably, the traditional OSC layer has a thickness of >20 nm, which usually hinders the direct interactions between the conductive channel and analytes. Extensive studies have proven that morphology optimization including controlled molecular orientation,[10–12] high crystallinity,[13,14] large grain boundary,[14,15] downscaling thickness[16] and porous structure[17] can improve the performance of organic-transistor-based sensors. These strategies, along with the development of molecular assembly methods and deposition techniques,[18–20] have boosted the use of flexible sensors in practical applications.

Here, we aim to outline the recent progress in OSC morphology-dependent chemical detection with transistor geometry and the latest advances in the construction strategies of the nano/microstructure of the OSC active layer. First, we introduce the sensing mechanism of these chemical sensors, to provide a deep understanding of the enhanced sensitivity and selectivity associated with OSC morphology. We then summary the key methods for controlling the morphology of organic thin films in recent processes. Notably, some processes in single-crystal layer fabrication have also been introduced to provide further suggestions on sensing modulation, which might be applied to large-area device fabrication with high mobility. Finally, we provide conclusions and future perspectives for the further development of chemical sensors with OSC film modulation.

2 Fundamentals of organic transistor based chemical sensors

Since the first organic thin film transistor was reported in 1987, they have been adopted as a feasible solution for sensitive chemical sensors that convert chemical information into electrical signals.[21,22] A traditional OFET consists of four active layers, including the gate electrode, source–drain electrodes, dielectric layer, and OSC layer (Fig. 1). When a gate voltage (V_{GS}) is applied, the carriers accumulate at the interface between the OSC and dielectric layer, and flow from

Danfeng Zhi

Danfeng Zhi received her BS degree from Anyang Normal University in 2015 and MS from Henan University in 2018, respectively. Since 2020, she has been at the School of Chemical Sciences in the University of Chinese Academy of Sciences (UCAS) for a Ph.D. degree. Her current research interest is focused on the fabrication and application of functional organic transistors.

Enyu Zhang

Enyu Zhang received his BS degree in chemistry from Jilin University in 2019. After that, he joined the School of Chemical Sciences, University of Chinese Academy of Sciences (UCAS) for a Master's degree. His current research interest is focused on developing organic field-effect transistors based on chemical/ biosensors.

Boya Zhang

Boya Zhang received her BS degree in chemical engineering and technology from the University of South China (2021). She joined the University of Chinese Academy of Sciences for a Master's degree in 2021. Her current research is focused on organic bioelectronics based on morphology modulation.

Fengjiao Zhang

Fengjiao Zhang received her Ph. D. degree from the Institute of Chemistry, Chinese Academy of Sciences (ICCAS) in 2015, and joined the UCAS in 2019 after her postdoctoral research in the University of Illinois at Urbana-Champaign. Her research interests include the fabrication, performance optimization and application development of organic bioelectronic devices.

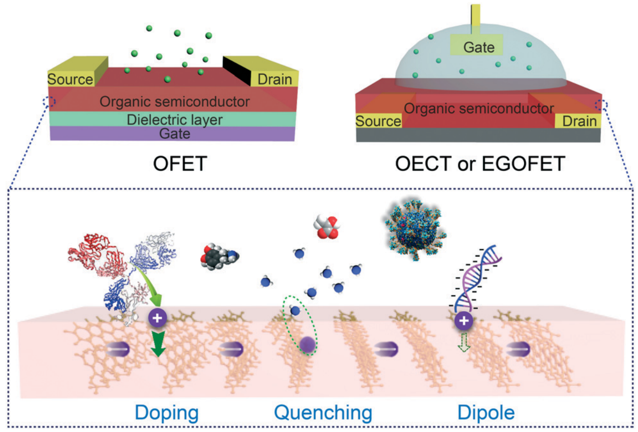

Fig. 1 Schematic illustration of organic transistor based chemical sensing. The device geometry shown here is an organic field effect transistor (OFET), an organic electrochemical transistor (OECT) and an electrolyte-gated OFET (EGOFET). In the semiconductive channel, the analytes can affect the carrier transport *via* doping, quenching or dipole interactions, *etc.*

the source to the drain electrode driven by V_{DS} in the conductive channel. The source–drain current (I_{DS}) can be controlled by modulating V_{GS} using the following equations:

$$I_{DS} = (W/L)\mu_{lin}C_{ox}(V_{GS} - V_{th})V_{DS}, \quad V_{DS} < V_{GS} - V_{th} \tag{1}$$

$$I_{DS} = (W/2L)\mu_{sat}C_{ox}(V_{GS} - V_{th})^2, \quad V_{DS} > V_{GS} - V_{th} \tag{2}$$

where μ is the carrier mobility at the saturation regime (μ_{sat}) and linear regime (μ_{lin}); L and W are the channel length and width, respectively; C_{ox} is the capacitance of the dielectric layer; V_{th} is the threshold voltage. In general, all changes in the active layers may cause I_{DS} fluctuations. In this section, we focus on the sensing mechanism caused by the stimuli directly triggered in OSC layers. The analytes interact with the OSC directly at the surface or at the conductive channel *via* diffusion into the bulk film. On the one hand, the OSC layer reacts with the analytes *via* chemical bond formation and total charge transfer, causing a change in carrier concentrations. On the other hand, weaker molecular interactions including hydrogen bonding, hydrophobic interactions and dipole–dipole interactions also induce changes in the carrier concentration with a partial charge transfer or trap-filling mechanism. These chemical interactions exhibit detectable changes in I_{DS}, V_{th} and μ. Recently, investigations have also demonstrated that the presence of chemicals may cause a signal response similar to that in a physical interaction, in which the chemical compounds disrupt carrier transport by expanding molecular stacking when diffusing through the OSC layers. Compared with traditional OFETs, electrolyte dielectric materials are used in EGOFETs. These transistors operate similarly to OFETs but with an electric double-layer formation near the dielectric/OSC interface. Consequently, the capacitance and carrier concentration can be several orders of magnitude higher, contributing to a fast signal response with a low operation voltage.

In comparison, OECTs operate through electrochemical doping, in which ions in the electrolyte media penetrate the semiconductor layer when the gate voltage is applied.[23–25] V_{GS} controls the conductivity of the OSC layer with redox state modulation and compensates for charge carrier formation. Transconductance (g_m) is the most commonly used parameter to describe OECT device performance, and it can be derived from $g_m = \partial I_{DS}/\partial V_{GS}$. According to the model proposed by Bernards *et al.*,[26,27] OECTs have an ionic circuit and an electronic circuit, which can describe the flow of ions and electronic charges, respectively. When the device operates at saturation, its electric characteristics can be quantitatively expressed using the following equation:

$$g_m = \frac{W}{L} d\mu C^*(V_{th} - V_{GS})(\text{depletion-mode}) \tag{3}$$

$$g_m = \frac{W}{L} d\mu C^*(V_{GS} - V_{th})(\text{accumulation-mode}) \tag{4}$$

where d is the thickness of the OSC layer and C^* represents the capacitance per unit volume of the channel. In this case, the effective capacitance depends on the thickness of the active layer, which leads to bulk doping. The parameter $d{\cdot}C^*$ is a parameter that can tune the performance and can be defined as the capacitance per unit area of the MOS capacitor.[24] Hence, the thickness of the OSC in the OECT plays a critical role in adjusting the trade-off relationship between the gain and bandwidth,[26] resulting in the modulation of the on/off ratio and switch speed. The morphology-dependent ion injection and carrier transport disorder also influence the intrinsic electric properties and operational physics of OECTs.[28–30] This ion-to-electron transistor is capable of efficiently amplifying the functions of chemicals, particularly compounds in aqueous environments, using electrolytes as gating media.[31]

2.1 Morphology dependent signal amplification in organic transistor based chemical sensing

In particular, the intrinsic amplification of a transistor is determined by its gain, which can be defined as g_m/g_0, where $g_0 = \partial I_{DS}/\partial V_{DS}$ is the output conductance. High-gain features are critical for the development of high-sensitivity sensors.[10] As the electronic coupling between neighbouring molecules, together with the energy-level shift, dominates the carrier transport speed and rate, which is governed by the molecular arrangement of the OSCs, the morphology of the OSC layers is important for determining the gain values and signal amplification functionality. In the past decades, considerable progress has been achieved in understanding the trade-off relationship between molecular stacking, including the orientation, alignment, packing density, and crystallinity, and the sensing performance by changing the contact injection and carrier transport.[9,15,32,33] First, carrier transport is mainly affected by ordered π–π stacking and an aligned backbone in the conductive channel inside the domains, and charge trapping at the grain boundary. Therefore, dense inter-molecular stacking and large overlapping of the π-conjugated backbone contribute to high mobility and stability in signal monitoring with organic transistors. Second, a high degree of edge-on stacking is regarded as a favourable orientation of the conjugated backbone for efficient two-dimensional carrier transport. In recent years, OSCs with face-on orientation and face-on/edge-on bimodal orientation have demonstrated high mobility, owing to the modulated energy barrier for carrier rejection and three-dimensional charge transport. Third, the high crystallinity and fewer intergrain regions contribute to the high mobility by reducing the number of traps. Thus, chemical sensing based on organic transistors has been promoted by enhanced device performance with optimized OSC molecular stacking. For instance, molecular design has been extensively applied to tune the backbone torsion and electronic structure, contributing to the enhancement of the hole/electron mobilities of OFETs.[20,34,35] These small molecules and polymers are promising candidates for chemical and biomolecular detection. In addition to synthetic approaches, surface engineering and post-treatment methods have been proposed to modulate the molecular stacking for sensitive chemical sensing. For example, poly(2,5-bis(3-tetradecylthiophen-2-yl)thieno[3,2-*b*]thiophene) (PBTTT) films with high crystallinity were developed *via* spin coating on an octyltrichlorosilane (OTS)-modified substrate, contributing to high mobility and good gas-sensing characteristics.[36]

2.2 Morphology dependent signal transition in chemical sensing

The physical and chemical interactions between the OSC layer and the analytes are key for controlling the sensitivity and selectivity of organic transistors. Generally, several requirements of the OSC active layers exist for efficient signal transition in chemical/biosensors (Fig. 2): 1) a suitable energy level to enable their reactivity with the analytes, 2) highly reactive sites and a large surface-area-to-volume ratio, which contribute to their charge transfer to the analytes, and 3) tunable dimensions with pores and boundary structures, which facilitate their direct access to analytes in the environment.

At the molecular level, molecular orientation is deemed to be a key factor in the reactions between transistors and chemicals. Previous reports revealed that the existence of a surface dipole built into the molecular layers of π-conjugated organic compounds can adjust the ionization potential of OSC molecules by up to 0.6 eV.[11,37] Based on this energy-level shift, several studies have demonstrated that molecular orientation can improve charge transfer at organic–organic heterojunctions. Moreover, the face-on orientation facilitates direct charge transfer with efficient π-core interactions. Recently, Zhang and Diao *et al.* constructed polymer OFETs with a precisely oriented conjugated backbone of a diketopyrrolopyrrole (DPP)-based conjugated polymer.[38] When the devices were treated with F_4-TCNQ, a larger mobility change was observed for devices with preferred face-on stacking in the polymer layer. The authors indicated that the face-on orientation contributed to host/dopant interaction sites and vertical charge transport, resulting in an enhanced electrical response when exposed to additional stimuli. Controlling the molecular stacking structure also facilitates sensitive and selective chemical sensing owing to the effective reaction at the sidechain. Zhang *et al.* fabricated selective CO and H_2S sensors based on DPP-based OFETs with a thymine group in the sidechain.[39] By controlling the edge-on stacking of the OSC molecules, Pd(II) and Hg(II) ions can be anchored at the interface of the thymine groups, which enables the formation of highly reactive sites on the semiconducting layer. Hence, the devices exhibited a sensitive response to CO and H_2S at low concentrations of 10 and 1 ppb, respectively.

The dimensional structure of the OSC layer is another critical factor that controls the sensing performance. Generally, thick and continuous films create diffusion barriers between the analytes and the conductive channel, resulting in poor sensor performance. Reducing film thickness is an effective way to expose the buried conductive layer to the analytes. This method has been reported for the construction of ultrathin (<10 nm) or monolayer-based films to improve the sensitivity, response time and recovery time of OFET-based chemical sensors.[40,41] Nevertheless, sensitive OECT sensors have not yet been developed because their sensing progress is relative to that of the bulk film. Moreover, ultrathin-film-based devices exhibit poor stability and low mobility, which impedes their long-term detection applications. Di and Zhu *et al.* demonstrated high-mobility NDI- and DPP-based OFETs with high-quality ultrathin films, which exhibited repeated sensitive responses and fast recovery for gases and biomolecules, respectively.[16,42–44]

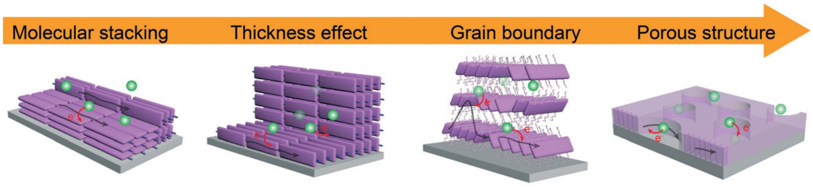

Fig. 2 Schematic illustration of multiscale morphology dependent carrier transport and signal transition in organic transistors. The grey arrow indicates the carrier transport in the channel, the dots represent analyte molecules and the red arrow presents charge transfer between analytes and OSC (taking electron doping as an example).

Manipulating the grain boundary is another approach for improving the sensitivities and detection limits of organic-transistor-based chemical detectors. A higher number of grain boundaries increase the structural defects, not only providing diffusion pathways for the analyte molecules but also creating a higher density of trap states in the channel. When the devices are exposed to chemical/bio-compounds, a higher sensing performance can be obtained easily. Someya *et al.* investigated the role of grain boundaries in OFET-based gas sensors with channel lengths varying from 2.5 to 45 μm.[45] The results indicated that, with a long channel length, the α,ω-dihexylquarterthiophene (DH4T) device responded to pentanol vapor, whereas the device demonstrated only a very small response with a short channel length and extremely large crystals. With further enlargement of the gaps in the active layer, pore formation allows effective contact and charge transfer between the conductive channel and the analyte species because of the larger surface-to-volume ratio (Fig. 3). Considering the decreased mobility caused by the damaged carrier-transport pathway, Diao *et al.* reported a series of DPP-based gas sensors with tunable nanopores ranging from 50 to 700 nm in the OSC layer.[46] The well-designed porous structure and ordered molecular stacking enabled high carrier transport and enhanced reactive sites for ammonia (Fig. 3b), leading to unprecedented ultrasensitive, ultrafast, and selective chemical sensing below 1 ppb. Jiang *et al.* further developed monolayer two-dimensional molecular crystals with porous structures to demonstrate good signal amplification properties.[47] This special film morphology consists of crystalline molecular stacking and a down-to-bottom conductive channel, enabling the direct detection of solid dopamine at a low concentration of 500 ppb (Fig. 3c). In the liquid sensor, the porous structure also facilitates molecule diffusion owing to the wetting condition. In the OECT based biosensor, for example, free-standing microporous scaffolds have been developed for the deposition of PEDOT:PSS.[48] These devices displayed ultrasensitive signal responses for dynamic and *in situ* measurements of 3D cell culture, which are attributed to ion penetration and effective reactions.[48,49] Marks *et al.* also developed the porous OSC layer *via* the breath figure process, enabling a signal response to various electrolytes (Fig. 3d).[50] Interestingly, the microstructure change of OSC layers is also promising for the sensitive and selective sensing of biomaterials *via* immobilizing receptors at the "gap" area for a shortened Debye length.[51–53] These results suggest that microstructure manipulation is an effective approach for realizing outstanding (bio)chemical sensing.

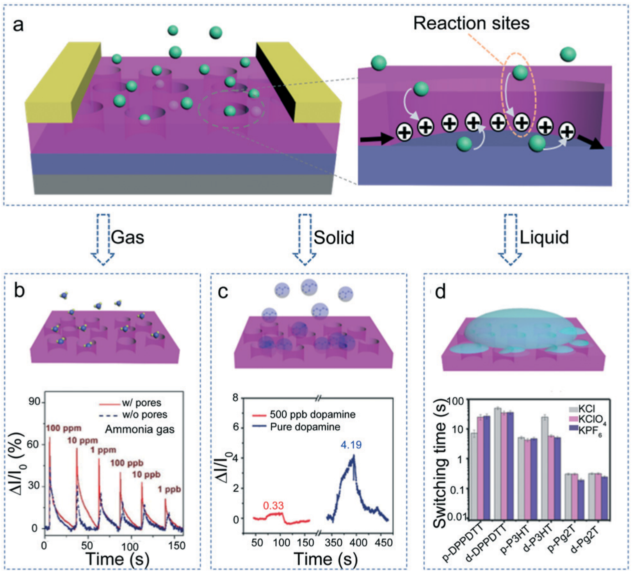

Fig. 3 (a) Device geometry of an organic transistor-based sensor with a porous active layer. The inset image exhibits the electric transfer between analyte molecules with the reaction sites in the channel. (b) Gas diffusion into the pore layer and current change of the ammonia sensor based on DPP2T-TT OFETs with (400 nm pore) and without pores. Reprinted from ref. 46. Copyright 2017 John Wiley and Sons. (c) Solid deposition on the porous layer. The bottom is the current response of nonporous and porous MMC OFETs when exposed to 500 ppb and pure dopamine powders. Reprinted from ref. 47. Copyright 2020 John Wiley and Sons. (d) Liquid immersed organic semiconductor layer, and the switching on time of the porous OECT device under different electrolyte solutions. Reprinted from ref. 54. Copyright 2021 John Wiley and Sons.

Considering the high quality of molecular stacking, assembled nanostrips or nanowires have been introduced to organic transistors to satisfy the requirements of efficient carrier transport and direct charge transfer with analytes. Müllen and Chi *et al.* adopted a dip-coating method to fabricate dendritic microstrips with 4–6 molecular layers based on dialkyl tetrathiapentacene (DTBDT-C6).[55] The microstructure grows continuously and is well aligned along the channel with a size of hundreds of micrometers. This nanoconfined structure has outstanding charge carrier mobility (>0.1 cm^2 V^{-1} s^{-1}) at the intra- or inter-molecular level. The ultrathin and microstructured OSC layer also provided a more efficient pathway for the interaction between OSC and ammonia, resulting in improved sensitivity and response/recovery time. To date, several types of nanostrip structures have been proposed as effective sensor candidates based on organic transistors.[56–58] For instance, Tang and Liu *et al.* developed OFETs based on CuPc single-crystalline nanowires and reduced the limit of detection for SO_2 to 0.5 ppm with a high sensitivity up to 119%.[56] Sung *et al.* further demonstrated a highly sensitive OFET sensor for ammonia using an array of single-crystal P3HT nanowires.[57] It is believed that the single-crystal nature and large surface-to-volume ratio of these nanostructures can be utilized in the OSC layer for electronic sensors.

3 Advanced strategies on the morphology control of OSCs' toward high sensing performance of organic transistors

Compared to the series of studies on organic transistor-based chemical sensors with different receptors and device structures,[2,8] the OSC morphology control exhibits a complex influence on both carrier transport and signal transition. As mentioned above, the morphology of OSC molecules involves intramolecular confirmation and intermolecular packing, mesoscale domain size, orientation, macroscale alignment and crystallinity.[59] The optimization of the chemical sensor requires a balance of multiscale morphologies to obtain high sensitivity, reliable specificity and suitable long-term stability. Herein, we summarize the following strategies for the construction of excellent organic-transistor-based sensors on the basis of favorable electrical properties.

3.1 Molecular design and exploration for designed molecular stacking

During molecular assembly, the conjugated molecules first nucleate and then grow under dynamic interactions between OSC molecules and OSC with the substrates.[18,59,60] Hence, the chemical structural features, including molecular size, rigidity, and heteroatoms on the backbones and sidechain groups, are the priority factors for precisely controlling multiscale morphology. As molecular stacking plays a critical role in carrier transport and charge transfer with additional signals, several reviews have summarized strategies for controlling multilevel film morphology by modifying the conjugated backbone and sidechains. Here, we briefly discuss the key roles of the molecular structure designs developed for organic-transistor-based sensors.

The planarity of the organic backbone is critical to induce the molecular stacking model and polycrystalline structure of the OSC layer. Early studies on altering the delocalized core structure of the small molecules and building blocks of polymers could regulate planar interchain and intrachain interactions, sequentially modifying the energy level.[61–64] Consequently, various degrees of morphology could be formed and the corresponding chemical responses could be obtained under exposure to analytes. In previous studies, substitution with F and Se atoms in the conjugated core would contribute to an interlocking interaction along the chains, causing backbone planarization and consequently increased π–π backbone interactions.[65,66] The resulting highly crystalline morphology yields high carrier transport and signal amplification. With this method, McCulloch *et al.* demonstrated an analogous regioisomeric polymer, pgBTTT, which displayed improved planarity highlighted by the S–O interaction.[67] The regiochemistry influences the polymer conformation and self-assembly, and subsequently optimizes the thin film morphology and electronic properties. The μC^* can reach 563 ± 33F $\mathrm{cm}^{-1}\ \mathrm{V}^{-1}\ \mathrm{s}^{-1}$, resulting in a large signal amplification function for OECT based sensors.

In addition to the aforementioned optimization of the backbone, introducing heteroatoms to the conjugated core can yield hydrogen bond interactions, contributing to the superstructure molecular assembly.[68] With relatively strong and highly directional noncovalent interactions, several OSC materials have demonstrated well-ordered stacking models for efficient carrier transport and long-term stability. Some organic pigments without soluble sidechain substitutions have demonstrated an interplay between strong π-stacking and H-bonding between molecules. In previous studies, DPPs, quinacridones, perylene diimides (PDIs) and indigos were developed as major OSCs in the construction of organic transistors for applications in chemical sensing.[69–72] For example, epindolidione and quinacridone are the H-bonded analogs of tetracene and pentacene (Fig. 4a), respectively, for which H-bonding is formed between –NH hydrogen atoms and carbonyl groups on adjacent molecules.[70] The interplay of H-bonding and π-stacking results in a significantly stable HOMO level and larger HOMO–LUMO gap relative to the acenes, contributing to a high air stability over a hundred days. The planar stacking structure of epindolidione enabled the OFET to have an excellent hole mobility up to 1.5 $\mathrm{cm}^2\ \mathrm{V}^{-1}\ \mathrm{s}^{-1}$. Furthermore, the well-aligned molecular stacking in the OSC layer along both the π–π stacking and H-bonding directions is proposed to realize the selective chemical detection. Diao *et al.* developed a new class of OSCs based on anticancer drugs, for which the molecular stacking alignments could be controlled *via* the meniscus-guided coating process.[73] They observed that the carrier mobility was correlated with the H-bond dihedral angles between ellipticine molecules, indicating a long-range electron/hole transport mechanism along the H-bonded molecular network. Interestingly, the well-designed molecular stacking enables the OFET to exhibit a high sensitivity of $\Delta I/I_0$ of over 8% at a concentration of 1 ppb, which is attributed to the formation of H-bonds between the carbonyl group of ethyl acetate and the amine moiety of ellipticine. The modulation of the hydrogen bonding interactions can be used to tune the crystalline domain and amorphous region in conjugated polymer films, which can further improve the mechanical properties of organic electronics.

Another strategic design for conjugated polymers involves the incorporation of copolymer blocks, non-conjugated units, or conjugation-break spacers to achieve morphological control with intrinsic stretchability (Fig. 4b). The key aspect for morphology and application manipulation is the balance between amorphous regions and crystalline domains. Bao *et al.* conducted a series of investigations on the molecular-structure-dependent stretchable electrical properties of proposed next-generation materials for applications in wearable sensors and integrated stretchable logic circuits.[74–76] As there are several reviews on this topic,[77–79] we will not introduce them in detail here.

Compared with the backbones, incorporating suitable sidechains facilitates fascinating applications by modulating the solubility, inter-molecular stacking, and crystallinity of the OSC layer (Fig. 4c). The chain length, sidechain attachment density, and branching sidechain have a significant impact on ordered molecular packing.[80–82] In chemical sensors, the alkyl chain contributes significantly not only by modulating the grain domain and boundary for analyte diffusion, but also through efficient reactions with analytes. For example, Kim *et al.* systematically investigated rylene diimide derivatives with perfluoroalkyl electron-withdrawing groups (EWGs) (Fig. 4c).[83] They observed that the molecular core with large delocalized LUMO π-electron

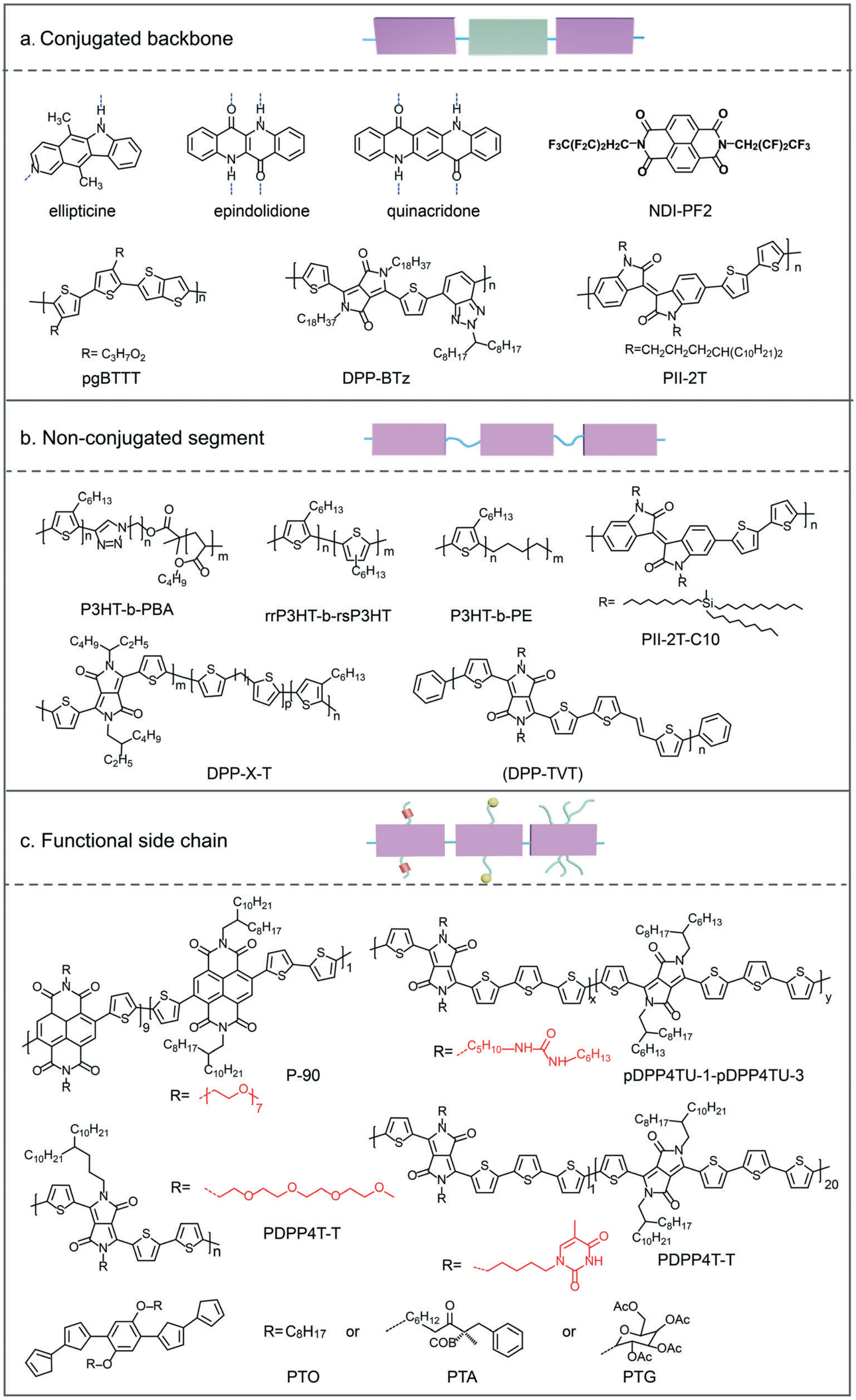

Fig. 4 Design roles and molecular structure of OSCs for morphology control. (a) Regulating the structure of the conjugated backbone, causing the tunable planarity and molecular interactions. (b) Introducing non-conjugated segments in the backbones, and (c) incorporating the side chain effect with functional groups.

density can trigger efficient charge transfer from ammonia to PDI-PF, leading to the formation of enhanced radical anions in the conductive film and sensitive ammonia detection. Zhang *et al.* also conducted a series of studies on the modification of sidechains in OSCs, resulting in the enhancement of charge transport and sensing functionality.[5] The first strategy is to change the asymmetric properties of the branching alkyl chain, which can reduce the changes in the molecular face-to-edge orientation.[84] The other is the induction of functional groups for enhanced molecular interactions. As such they introduced urea groups in the diketopyrrolopyrrole (DPP)–quaterthiophene conjugated polymer, which facilitates the interconnection of the polymer domain *via* the H-bonding of the urea groups in the side chains.[85] When the molar ratio between the urea-containing alkyl chain and the branching alkyl chain was 1 : 10 (named as pDPP4TU-1–pDPP4TU-3), the width of the thick nanofibers in the film increased from 30 to ~50 nm, contributing to an average mobility of 11.4 cm^2 V^{-1} s^{-1}. The devices also displayed an increased sensitivity to ammonia. The modification of the conjugated polymer with thymine[39] and tetra(ethylene glycol) groups[86] in the sidechain contributed to a sensitive, selective, and fast response to CO and alcohol vapor, respectively. Another interesting study involved the addition of *tert*-butoxycarbonyl groups to the sidechain,[87] which can be cleaved at 240 °C under vacuum. The release of gaseous isobutylene results in the formation of pinhole structures, thereby contributing to the sensitive and selective detection of ammonia and amines. In OECT devices, the incorporation of hydrophilic glycol and charged ionic sidechains is regarded as a widely accepted method for OSC synthesis, which can induce microphase separation and separate carrier and ion transport.[6,88,89] For instance, copolymer P-90 can facilitate an interaction with the enzyme and enhance the water uptake capacity of the polymer.[90] This material has been widely used for the aqueous detection of lactate and glucose.[91,92]

3.2 Advanced process techniques for nano-/micro-structure modulation

Vapor deposition and solution-processing techniques have been widely investigated for morphology control in OSC deposition. A simple optimization of the processing conditions can cause a marked morphological transition and a change in the sensing performance. Here, we summarize several advanced techniques for the nano-/microstructure modulation of OSC layers.

The nano-/microstructure of OSCs can be formed during or after the deposition process. Previously, Torsi and Katz *et al.* varied the thin-film morphologies of organic transistors fabricated with different α-thiophene oligomer derivatives, for which the grain size was tuned by changing the substrate temperature during vacuum deposition.[94] To induce the 2D growth of pentacene, Oh and Cho *et al.* used bis(triphenylsilyl)benzene (TSB3) as a surface inducer in thermal deposition.[93] As shown in Fig. 5a, pentacene was sequentially deposited on a substrate that had been deposited with TSB3, which has a low T_g, and heated at 60 °C during OSC deposition. Interestingly, the low T_g and structural features of TSB3 molecules induced agglomeration on the OTS-treated substrate owing to surface tension. In this case, pentacene was first adsorbed onto the rubbery TSB3 film instead of the dewetted OTS area, leading to a morphology with far fewer grain boundaries and myriad nanometer-sized pores (Fig. 5b and c). Grazing incidence X-ray diffraction analysis also demonstrated that the sequentially evaporated pentacene on TSB3 was predominantly in the thin-film phase, whereas the pentacene film deposited without TSB3 had both thin-film and bulk phases (Fig. 5d). This high-quality 2D porous structure enabled

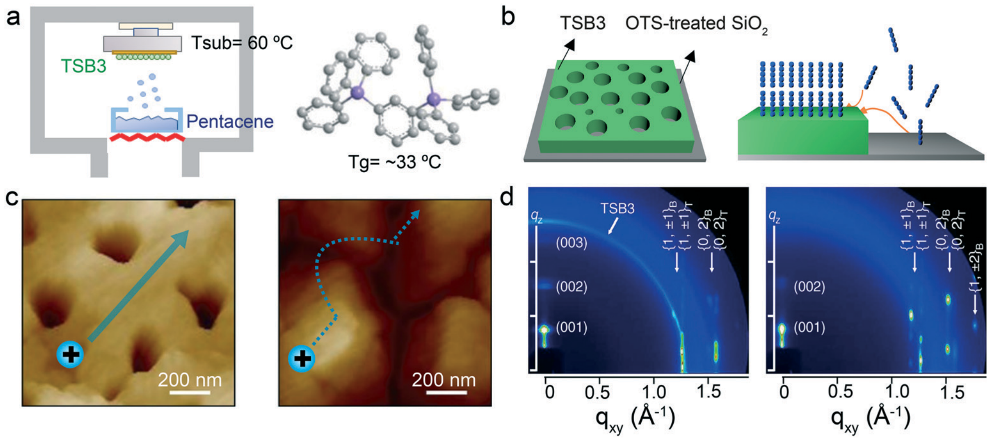

Fig. 5 (a) Schematic illustration of sequentially depositing TSB3 and pentacene. The substrate was heated to 60 °C during the deposition. The TSB3 molecular structure is shown in the right. (b) Mechanism of the growth of pentacene on the OTS substrate with a TSB3 layer. (c) AFM images of pentacene/TSB3 and pentacene on the OTS-modified substrate. Scale bar: 200 nm. (d) GIXD images of the pentacene film with and without TSB3. Reproduced under the terms of the CC-BY Creative Commons Attribution 4.0 International License (**https://creativecommons.org/licenses/by/4.0/**) from ref. 93. Copyright 2017 Springer Nature.

the OFET to have a high mobility up to 6.3 cm^2 V^{-1} s^{-1} and a significant response to methanol gas. The microstructure of the OSC layer can also be constructed *via* post-treatment. For example, imprinting treatment after film deposition can create a patterned structure as designed. Sun and Huang *et al.* proposed a Blu-ray movie disc as a nanoimprinting template and developed a quasi-random arrangement of islands and pits on a polymer semiconductor layer.[95] The imprinted films exhibited fascinating optoelectrical properties that could be employed for effective chemical sensing. Recently, Andrew *et al.* have also demonstrated a 3D-like conductive fiber by vapor-coating a silk fabric.[96] This structured fiber was used in the construction of an OECT that displayed a high on/off ratio of 100 and a g_m value of 100 µS at zero gate voltage. Its excellent performance enables its application in low-power-consumption integrated circuits and wearable electronic biosensors.

As mentioned above, the film thickness is important for manipulating the sensing performance of organic-transistor-based chemical sensors. The spin-coating method is a traditional process for OSC deposition. In general, solvent quality, solution concentration, rotation speed, and substrate treatments can affect the solvent evaporation dynamics, OSC–substrate interactions, and the time scale for OSC aggregation, resulting in changes in the film thickness and microstructure. Considering the hydrophobic OTS modification, an advanced spin-coating method was proposed to realize the deposition of ultrathin high-quality monolayer or bilayer films. This process is called the on-the-fly dispensing spin-coating process.[42] In this process, a solution droplet is added to a rotated substrate (Fig. 6a). The tangential force of rotation can overcome the dewetting issues and enable the deposition of an ultrathin film on the OTS-modified SiO_2 surface. The film thickness of NDI3HU-DTYM2 and NDI(2OD)(4*t*-BuPh)-DTYM2 can be successfully modulated from >80 nm to 1–3 molecular layers by varying the rotation speed (Fig. 6b). The ultrathin film directly exposes the conductive channel to the analytes, yielding sensitive and fast-responsive sensing signals (Fig. 6c). Similarly, Bao *et al.* demonstrated an off-center spin-coating method by placing the substrate aside from the center of the spin coater, resulting in a well-aligned and highly crystalline OSC thin film.[97]

Meniscus-guided coating has been developed in the past decades to control molecular stacking and film

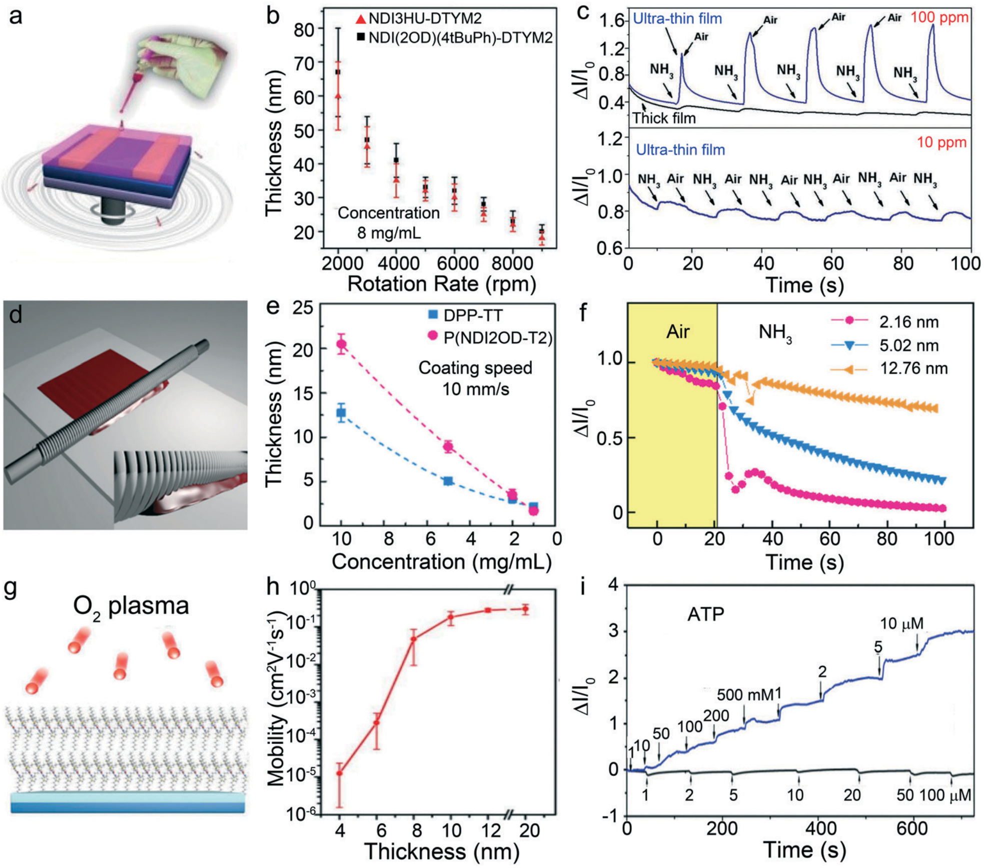

Fig. 6 (a) Illustration of the on-the-fly-dispensing spin-coating process, and the corresponding (b) thickness of NDI3HU-DTYM2 and NDI(2OD)(4*t*-BuPh)-DTYM2 films as a function of the rotation rate. (c) Current response to ammonia of NDI(2OD)(4*t*-BuPh)-DTYM2 based thin-film and ultrathin film transistors. Reproduced from ref. 42. Copyright 2013 John Wiley and Sons. (d) Schematic illustration of the bar-coating process. (e) Thickness of DPP-TT and P(NDI2OD-T2) films as a function of solution concentration with bar coating. (f) Sensing sensitivity of DPP-TT OFET with different film thicknesses during the NH_3 detection process. Reproduced from ref. 40. Copyright 2016 John Wiley and Sons. (g) Schematic illustration of the *in situ* physical etching process with plasma treatment. (h) Mobility of PDPP3T OFETs change as a function of plasma treatment time. (i) Current change of the apyrase functionalized OFET with exposure to ATP solution. Reproduced from ref. 44. Copyright 2018 RSC Publisher.

nanostructure. The blade properties, substrate condition, solvent and solution concentration, and additional fields (such as temperature and electric filed) support multi-level morphology regulation.[19,98–102] For instance, Noh *et al.* demonstrated an effective approach toward the deposition of ultrathin polymer films with molecular-level precision (Fig. 6d).[40] A wire-wound bar was used to control the polymer ink wet-coated onto the substrate along a fixed substrate with less material waste. The film thickness can be controlled by changing the coating speed, the structure of the wound wire, and solution concentration. As shown in Fig. 6e, the films thickness was confined between 2–13 nm for DPP2T-TT and 2–20 nm for P(NDI2OD-T2) (also named as N2200). The crystalline microstructure of the ultrathin films endowed the corresponding device with an increased signal response with decreasing film thickness (Fig. 6f).

Compared with deposition techniques, post-treatment techniques, such as the physical etching method, can reduce the thickness of the OSC layer effectively (Fig. 6g and h). Di and Zhu *et al.* developed a molecular-antenna-tailored OFET using a plasma-assisted interfacial grafting method.[44] When the etching power increased, the film thickness decreased with the removal of the surface layer. By controlling a neighboring-conductive-channel layer of poly-(diketopyrrolopyrrole-terthiophene) (PDPP3T), they demonstrated sensitive and selective adenosine triphosphate (ATP) monitoring with a minimized molecular gap between the analyte and surface receptors (Fig. 6i). However, this process damages the OSC layer and results in decreased mobility (Fig. 6h), which should be mitigated for real applications.

3.3 Surface engineering enabled patterned morphology deposition

Surface engineering plays a vital role in multiscale molecular stacking in organic-transistor-based chemical detection. The surface energy difference between the substrate and the OSCs can affect the cohesive interaction and molecular aggregation

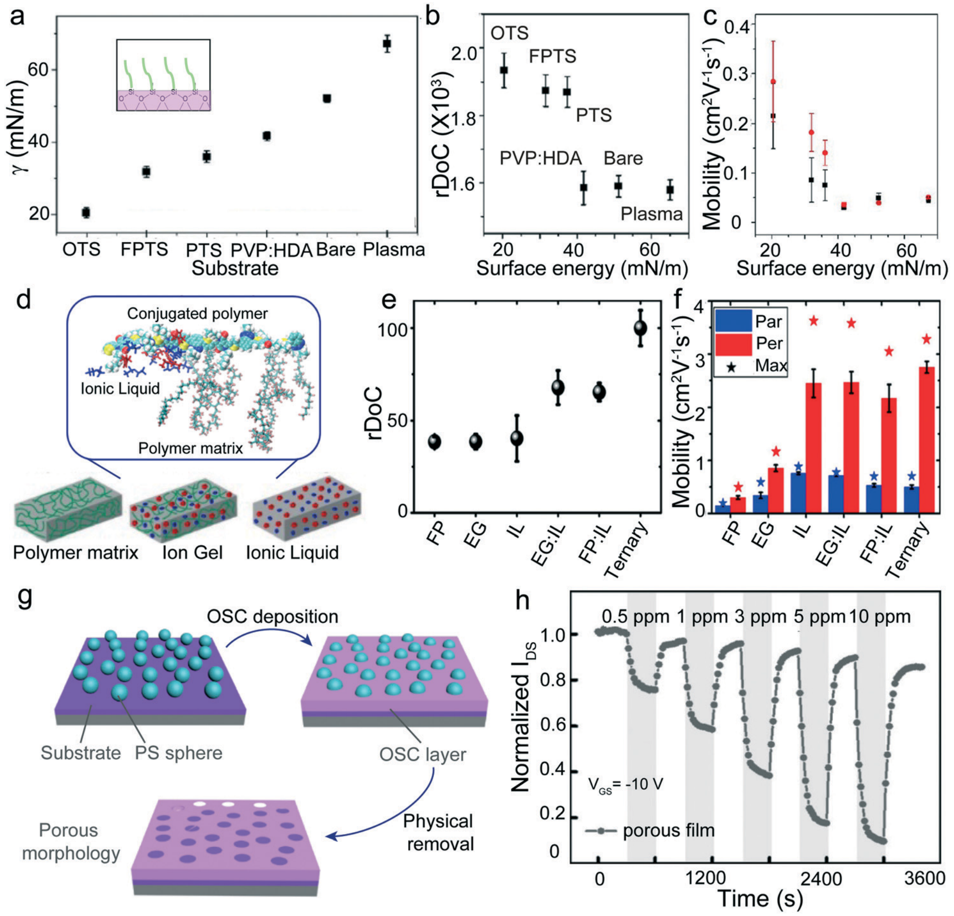

Fig. 7 Methods developed for surface treatments on morphology control for sensing. (a) Surface energy values for silicon substrates treated with OTS, FPTS, PTS, PVP:HDA, and plasma. Reproduced from ref. 103. Copyright 2018 American Chemical Society. (b) Relative degree of crystallinity (rDoc) of DPP2T-TT films and (c) carrier mobilities of corresponding OFETs changed as a function of surface energy for OSC deposition. (d) Schematic illustration of ion–π interactions at the dynamic template surface in the solution process. (e) rDoC of DPP-BTz films and (f) corresponding mobility of OFETs with films coated on various templates. Reproduced from ref. 107 and 109. Copyright 2019 and 2020, American Chemical Society. (g) PS nanoparticle modified surface for porous DNTT film formation, and (h) current change of porous DNTT OFETs to ammonia in the concentration from 0.5 ppm to 10 ppm. Reproduced from ref. 17. Copyright 2017 John Wiley and Sons.

in the morphology. Chung *et al.* constructed a PBTTT-based gas sensor by inserting a modification layer on the substrate, and thus obtained an optimized OSC layer with a large surface area and percolation pathways for charge carriers.[36] The resulting OFETs could achieve a high sensitivity and timely response to ammonia exposure at concentrations as low as 10 ppm. Diao *et al.* also systematically investigated the surface-energy-dependent polymeric morphology by introducing OTS-, phenyltrichlorosilane- (PTS-), pentafluorophenylpropyltrichlorosilane- (FPTS-) self-assembly monolayer, poly(4-vinylphenol):4,4′-(hexafluoroisopropylidene)-diphthalic anhydride (PVP:HDA), bare and plasma-treated surfaces (Fig. 7a).[103] The in-depth morphology and device characterization demonstrated that decreasing the substrate surface energy can increase the thin-film crystallinity, the degree of molecular ordering and the extent of domain alignment (Fig. 7b), by reducing the polymer nucleation barrier on the substrates. The morphology resulted in an order of magnitude increase in carrier mobility from 0.03 to 0.3 $cm^2\ V^{-1}\ s^{-1}$ (Fig. 7c). Furthermore, the modified substrate surface can be treated with a patterned structure using oxygen plasma or a photolithography process. For instance, the hydrophobic cross-linked PVP layer was treated with ultraviolet-ozone (UVO) treatment under a shadow mask for 10 min, resulting in a methyl group/hydrophobic-patterned surface.[104] Thereafter, the misorientation of 6,13-bis(triisopropylsilylethynyl)pentacene (TIPS-pentacene), was induced by the contact line curvature at the surface energy patterned surface in meniscus-guided coating. These patterned thin films (with different thickness) can be further applied for achieving sensitive and fast responses to chemical compounds.

Aside from the surface energy induced nucleation control at the interface, the molecular interactions induced between the substrate and the conjugated semiconductors demonstrated a specific way for controlling the film morphology. Graphene is well studied as a modification layer in controlling molecular growth owing to the π–π interaction and van der Waals interactions. For instance, P3HT can display a combined edge-on and face-on configuration, whereas the molecules only aggregate into an edge-on configuration on indium tin oxide.[105] On the other hand, elastic, dipole, and H-bond interactions facilitate molecular stacking in organic transistors owing to weak interaction-driven forces. Diao *et al.* developed a dynamic-template induced meniscus-guide coating approach, in which the ionic or hydrogen-bonded liquid is mixed in the polymer matrix or held in the porous layer (Fig. 7d).[106–108] The dynamic template can direct polymer assembly by providing strong ion–π interactions at the assembly interfaces, yielding highly aligned and crystalline polymer thin films.[108] They further studied the dynamic template created multivalent interactions with conjugated polymers by using a fluoropolymer, hydrogen-bonded liquid and ionic liquid.[109] The results demonstrated that the multicomponent dynamic template could lead to a 50–150% improvement in the relative degree of crystallinity and 2–5 times chain alignment and a high hole mobility of up to 3.6 $cm^2\ V^{-1}\ s^{-1}$ (Fig. 7e and f). Based on the dynamic substrate, the same group realized the molecular orientation change between face-on and edge-on stacking for a series of organic polymers, leading to efficient interface charge transfer for chemical sensing. For instance, the well-controlled face-on-orientated poly[[2,5-bis(2-octadecyl)-2,3,5,6-tetrahydro-3,6-diketopyrrolo-[3,4-*c*]pyrrole-1,4-diyl]-*alt*-(2-octylnonyl)-2,1,3-benzotriazole] (DPP-BTz) films can enrich the reaction sites with F_4-TCNQ at the film surface,[38] resulting in increased carrier mobility under enhanced charge transfer and trap filling through vertical molecular coupling. On the other hand, the highly ordered, aligned, and uniform continuous 2D monolayer film successfully grown on the dynamic template exhibited distinct electronic structures, which resulted in a measurable charge transport property compared with the reference films.[110] This electrical characterization of the 2D monolayer allows an over 85% current change to 1 ppb ammonia. There are several reports on forming porous structures through surface modification with polystyrene (PS) nanoparticles or nanoporous anodic alumina.[111,112] In these reports, the PS nanoparticles could be deposited on a substrate modified with a PS thin layer or grafted *via* freeze-drying. After the deposition of the OSC materials, the PS nanoparticles were removed *via* physical processes, such as wet etching (Fig. 7g). In Huang's report, the resulting porous morphology of the OSC layer could reach the level of sub-100 nm to >1 μm, yielding a sensitive and fast response to chemical compounds (Fig. 7h).[17] Notably, the microstructure prepared with this template is limited by the assembly structure of the PS nanoparticles, which is attributed to the nanoparticle size, surface properties, dispersion uniformity, substrate condition and bottom-up approach.

3.4 Nanoparticle or blend additions induced microstructure construction

Phase separation by employing a mixture solution with nanoparticle addition or OSC addition is an alternative method to control the nano-/microstructural morphology. As representative examples, water vapor particles have been widely used in porous formations, known as breath figures, in the conjugated polymers used in OFET and OECT devices. In this method, water droplets can be generated by directing aqueous vapor on a cold surface, resulting a humid environment and porous structure after evaporating the water condensation (Fig. 8a).[50] Recently, Facchetti, and Marks *et al.* have adopted a porous small molecular and polymeric layer, and subsequently performed the breath figure process.[54] For example, the pore structure can be achieved on the spin-coated N2200/PS blend and C_8-BTBT/PS blend layers, contributing to sensitive gas detection (Fig. 8b–d). The pore size can be modulated from 200–1000 nm with a depth of ∼65 nm for p-DPPDTT, ∼45 nm for P3HT and ∼55 nm for p-Pg2T-T films, respectively. It should be noted that the

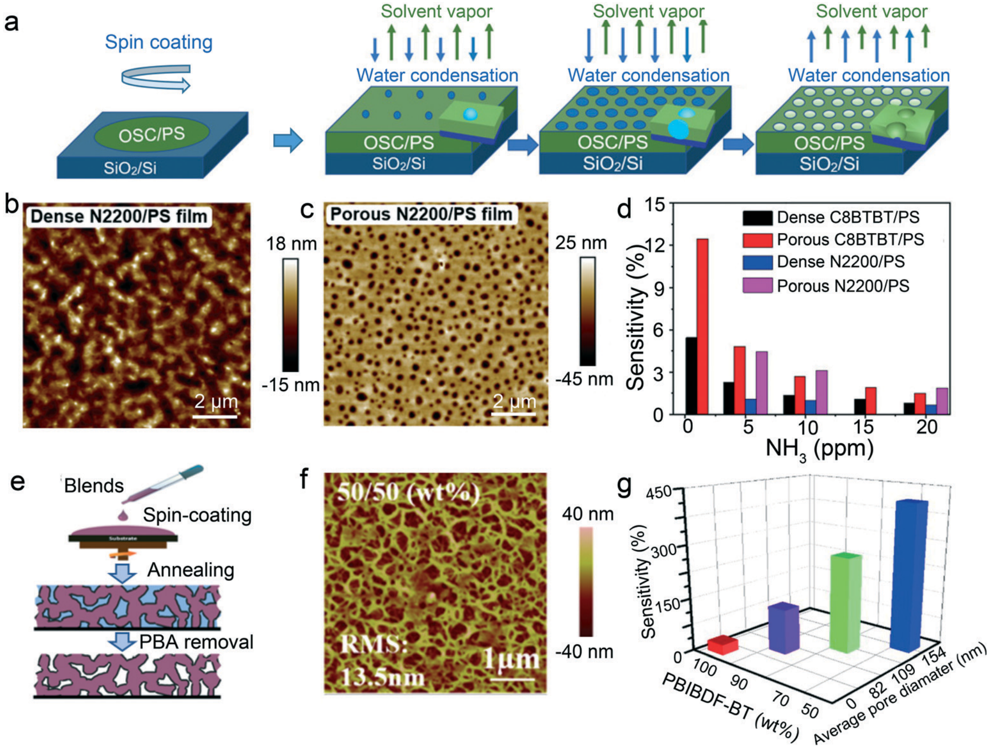

Fig. 8 Macrostructure control with a mixture solution. (a) Schematic illustration of porous film formation *via* the breath figure method, in which the water-vapor particles are formed by controlling humidity. (b and c) AFM images of surface morphology for dense N2200 film and porous N2200 film. (d) Sensitivity of corresponding devices with and without pores as a function of ammonia gases. Reproduced from ref. 50. Copyright 2020, the authors, some rights reserved; exclusive licensee AAAS. Distributed under a Creative Commons Attribution NonCommercial License 4.0 (CC BY-NC). (e) Schematic illustration of microporous film formation with spin-coated blend solution. The PBA addition was solvent washed after phase separation in the coating process. (f) AFM images of PBIBDF-BT/PBA blend films washed with acetone. (g) Sensitivity of the 3D porous film dependent organic transistor to humidity. Reproduced from ref. 117. Copyright 2017 American Chemical Society.

random pores formed in the semiconductive layer are attributed to the greater intermolecular force in the π-backbone and rapid solidification under the spin-coating and solvent evaporation processes. Although strategies have been developed for controlling porous structures with the breath figure approach, the requirement of a high-humidity environment impedes its application, particularly for n-type devices with high mobility and stability.

Compared with the breath figure method, phase separation with an OSC/insulating polymer mixture and polymer/small additions provides a more controllable porous structure by changing the deposition conditions.[113–116] The mechanism of this process is the immiscibility during the solution-coated deposition. As shown in Fig. 8e, Qiu *et al.* blended several organic polymers with a low-M_w polymer poly-(1,4-butylene adipate) (PBA) and deposited the films *via* the spin-coating method.[117] There is a phase separation during spin-coating which forms a microphase morphology. The 2D or 3D porous morphology was obtained after washing PBA with acetone. By varying the compound percentage, a polymer film with well-ordered nanostructures was achieved, with various pore sizes ranging from 82 to 154 nm (Fig. 8f).[117] The optimized microstructure plays the critical role in the signal response to water. The well-ordered nanostructures have been used in constructing humidity sensors that exhibited a sensitivity of 415 and a response time of 0.68 s when the humidity changed from 32% to 69% (Fig. 8g).

Conclusions and perspective

The structure of OSCs—which are the key compounds in organic transistors—ranging from atomic to microstructural and mesoscopic scales, plays a critical role in manipulating the electrical properties of the device, and its application in chemical sensing. The understanding of how the morphology controls the sensing performance has led to the development of chemical and biological sensors for use in different fields. Corresponding devices deserve continuous efforts to identify the advances and potential towards realistic applications, from the perspectives of sensing performance and operation stability in various environments, such as the physiological fluid, high-humidity environment, extremely cold/hot conditions, *etc.* Although sensing-oriented molecular stacking and microstructural optimization of the OSC layer have experienced rapid development over the past decades, challenges remain to achieve these realistic applications in daily life.

First, the outlined experiments and reviews delineate a roadmap for controlling molecular aggregation at different length scales; however, considerable efforts have to be made to produce a fully consistent methodology for tuning the sensing parameters. For example, dense and ordered molecular stacking contributes to high mobility but always results in a low sensitivity and long response time. In addition, the operating stability and reproducibility are impeded by the increased surface roughness and porous structure, which allow efficient analyte diffusion and a large surface-to-area ratio. Therefore, a deeper understanding of the physical process of the carrier transport and molecular interactions within the conductive channel is necessary to guide the construction of chemical sensors. Considering the advantages of the facile processability of OSCs, fine-tuned nanostructures in the active layer should be considered during deposition and/or post-treatment. It is also important to incorporate the assembly of receptors with the multiscale morphology modulation of the OSC layer, leading to remarkable sensitivity and selectivity of organic-transistor-based chemical sensors.

Second, the mechanical properties and sensing performance of flexible chemical sensors should be fine-tuned as desired, but the roles played by the OSC morphology are still not apparent. Existing organic-transistor-based chemical sensors have been demonstrated to be successful in static signal collection—for example, commercial gas sensors for house renovation. The *in situ* detection of chemical or biological species under bending or stretching has attracted increasing attention. Universal techniques to facilitate the fabrication of mechanically robust transistors with well-designed morphologies need to be particularly explored. For these flexible devices, it is expected that the stretched OSC layer can enhance the chemical sensing performance owing to the enlarged grain boundaries, reduced Debye screening length, and increased reaction sites. Interestingly, studies have demonstrated that the deformed graphene channel can yield the ultrasensitive detection of nucleic acids,[52,53] which is attributed to the nanoscale deformation-induced "electrical hot spots" in the sensing channel of field-effect biosensors. This highlights the need for future investigations of stretchable chemical/biosensors with unpredicted morphology modulation. Moreover, systematic studies on the dynamic changes in the film morphology and electrical response are of particular importance for improving the repeatability and reliability of organic electronic sensors.

Recently, the construction of implantable biosensors for personal healthcare has attracted significant interest. The biocompatibility and biodegradability of the OSC layers, when attached to biological organs, are the dominant factors facilitating their application in this field. To fulfill this requirement, biosegments or bioactive groups have been incorporated into OSC derivatives. Hence, the morphology can be tuned according to the following aspects: 1) suitable polycrystallinity and microphase separation can promote carrier and/or ion transport in the devices, and 2) the desired molecular orientation for the preferred chemical features of the OSC-layer surface enables the reaction sites to be directly exposed to the analytes. Further efforts are required to redefine the structural and functional properties in the physiological environment. Moreover, there are still important challenges in further understanding the operation stability in the physiological environment, which can give more suggestions on the molecular arrangement and film morphology of OSCs in organic transistors.

In summary, tremendous progress has been made in organic transistor-based chemical sensors. However, realizing realistic applications will require much more progress. In this review, we summarized the fundamentals of OSC morphology guided chemical sensing with organic transistors, and discussed key processing strategies to control the multiple-length-scale morphology through molecular design, technique optimization, substrate engineering and blend/addition usage. We expect a boost in the development of morphology-guided organic electronics in the near future.

Conflicts of interest

There are no conflicts to declare.

Acknowledgements

This research was financially supported by the Natural Science Foundation of Beijing (4202077), the National Natural Science Foundation of China (21905276, 6197396), the Strategic Priority Research Program of Chinese Academy of Sciences (XDPB13), the Fundamental Research Funds for the Central Universities (E1E40301X2) and CAS (ZDBS-LY-SLH034).

References

1 M. Y. Lee, H. R. Lee, C. H. Park, S. G. Han and J. H. Oh, *Acc. Chem. Res.*, 2018, **51**, 2829–2838.
2 M. Magliulo, K. Manoli, E. Macchia, G. Palazzo and L. Torsi, *Adv. Mater.*, 2015, **27**, 7528–7551.
3 S. G. Surya, H. N. Raval, R. Ahmad, P. Sonar, K. N. Salama and V. R. Rao, *TrAC, Trends Anal. Chem.*, 2019, **111**, 27–36.
4 A. M. Pappa, O. Parlak, G. Scheiblin, P. Mailley, A. Salleo and R. M. Owens, *Trends Biotechnol.*, 2018, **36**, 45–59.
5 Z. Liu, G. Zhang and D. Zhang, *Acc. Chem. Res.*, 2018, **51**, 1422–1432.
6 E. Zeglio and O. Inganas, *Adv. Mater.*, 2018, **30**, 1800941.
7 X. Wu, S. Mao, J. Chen and J. Huang, *Adv. Mater.*, 2018, **30**, 1705642.
8 J. Wang, D. Ye, Q. Meng, C. A. Di and D. Zhu, *Adv. Mater. Technol.*, 2020, **5**, 2000218.
9 S. Zhang, Y. Zhao, X. Du, Y. Chu, S. Zhang and J. Huang, *Small*, 2019, **15**, e1805196.
10 F. Torricelli, L. Colalongo, D. Raiteri, Z. M. Kovacs-Vajna and E. Cantatore, *Nat. Commun.*, 2016, **7**, 10550.
11 S. Fabiano, H. Yoshida, Z. Chen, A. Facchetti and M. A. Loi, *ACS Appl. Mater. Interfaces*, 2013, **5**, 4417–4422.
12 R. Joseph Kline, M. D. McGehee and M. F. Toney, *Nat. Mater.*, 2006, **5**, 222–228.

13 R. Steyrleuthner, R. Di Pietro, B. A. Collins, F. Polzer, S. Himmelberger, M. Schubert, Z. Chen, S. Zhang, A. Salleo, H. Ade, A. Facchetti and D. Neher, *J. Am. Chem. Soc.*, 2014, **136**, 4245–4256.

14 R. Noriega, J. Rivnay, K. Vandewal, F. P. Koch, N. Stingelin, P. Smith, M. F. Toney and A. Salleo, *Nat. Mater.*, 2013, **12**, 1038–1044.

15 J. Locklin and Z. Bao, *Anal. Bioanal. Chem.*, 2006, **384**, 336–342.

16 Y. P. Zang, D. Z. Huang, C. A. Di and D. B. Zhu, *Adv. Mater.*, 2016, **28**, 4549–4555.

17 J. Lu, D. Liu, J. Zhou, Y. Chu, Y. Chen, X. Wu and J. Huang, *Adv. Funct. Mater.*, 2017, **27**, 1700018.

18 Z. Lu, C. Wang, W. Deng, M. T. Achille, J. Jie and X. Zhang, *J. Mater. Chem. C*, 2020, **8**, 9133–9146.

19 Y. Diao, L. Shaw, Z. Bao and S. C. B. Mannsfeld, *Energy Environ. Sci.*, 2014, **7**, 2145–2159.

20 K. S. Park, J. J. Kwok, R. Dilmurat, G. Qu, P. Kafle, X. Luo, S. H. Jung, Y. Olivier, J. K. Lee, J. Mei, D. Beljonne and Y. Diao, *Sci. Adv.*, 2019, **5**, eaaw7757.

21 A. Tsumura, H. Koezuka and T. Ando, *Appl. Phys. Lett.*, 1986, **49**, 1210–1212.

22 H. Sirringhaus, *Adv. Mater.*, 2014, **26**, 1319–1335.

23 J. T. Friedlein, R. R. McLeod and J. Rivnay, *Org. Electron.*, 2018, **63**, 398–414.

24 J. Rivnay, S. Inal, A. Salleo, R. M. Owens, M. Berggren and G. G. Malliaras, *Nat. Rev. Mater.*, 2018, **3**, 17086.

25 M. Zhu, P. Li, J.-L. Li and T. Lei, *Mol. Syst. Des. Eng.*, 2022, **7**, 6–20.

26 J. Rivnay, P. Leleux, M. Ferro, M. Sessolo, A. Williamson, D. A. Koutsouras, D. Khodagholy, M. Ramuz, X. Strakosas, R. M. Owens, C. Benar, J. M. Badier, C. Bernard and G. G. Malliaras, *Sci. Adv.*, 2015, **1**, e1400251.

27 D. A. Bernards and G. G. Malliaras, *Adv. Funct. Mater.*, 2007, **17**, 3538–3544.

28 J. T. Friedlein, J. Rivnay, D. H. Dunlap, I. McCulloch, S. E. Shaheen, R. R. McLeod and G. G. Malliaras, *Appl. Phys. Lett.*, 2017, **111**, 023301.

29 A. Laiho, L. Herlogsson, R. Forchheimer, X. Crispin and M. Berggren, *Proc. Natl. Acad. Sci. U. S. A.*, 2011, **108**, 15069–15073.

30 A. Giovannitti, D. T. Sbircea, S. Inal, C. B. Nielsen, E. Bandiello, D. A. Hanifi, M. Sessolo, G. G. Malliaras, I. McCulloch and J. Rivnay, *Proc. Natl. Acad. Sci. U. S. A.*, 2016, **113**, 12017–12022.

31 A. Yang and F. Yan, *ACS Appl. Electron. Mater.*, 2020, **3**, 53–67.

32 L. Huang, Z. Wang, X. Zhu and L. Chi, *Nanoscale Horiz.*, 2016, **1**, 383–393.

33 L. Wang, D. Fine, D. Sharma, L. Torsi and A. Dodabalapur, *Anal. Bioanal. Chem.*, 2006, **384**, 310–321.

34 J. Lee, H. Ko, E. Song, H. G. Kim and K. Cho, *ACS Appl. Mater. Interfaces*, 2015, **7**, 21159–21169.

35 M. S. Chen, J. R. Niskala, D. A. Unruh, C. K. Chu, O. P. Lee and J. M. J. Fréchet, *Chem. Mater.*, 2013, **25**, 4088–4096.

36 S. H. Yu, J. Cho, K. M. Sim, J. U. Ha and D. S. Chung, *ACS Appl. Mater. Interfaces*, 2016, **8**, 6570–6576.

37 S. Duhm, G. Heimel, I. Salzmann, H. Glowatzki, R. L. Johnson, A. Vollmer, J. P. Rabe and N. Koch, *Nat. Mater.*, 2008, **7**, 326–332.

38 F. J. Zhang, E. Mohammadi, G. Qu, X. J. Dai and Y. Diao, *Adv. Mater.*, 2020, **32**, 2002823.

39 Y. Yang, Z. Liu, L. Chen, J. Yao, G. Lin, X. Zhang, G. Zhang and D. Zhang, *Chem. Mater.*, 2019, **31**, 1800–1807.

40 D. Khim, G. S. Ryu, W. T. Park, H. Kim, M. Lee and Y. Y. Noh, *Adv. Mater.*, 2016, **28**, 2752–2759.

41 S. Cui, H. Pu, S. A. Wells, Z. Wen, S. Mao, J. Chang, M. C. Hersam and J. Chen, *Nat. Commun.*, 2015, **6**, 8632.

42 F. J. Zhang, C. A. Di, N. Berdunov, Y. B. Hu, X. K. Gao, Q. Meng, H. Sirringhaus and D. B. Zhu, *Adv. Mater.*, 2013, **25**, 1401–1407.

43 Y. Zang, F. Zhang, D. Huang, C. A. Di, Q. Meng, X. Gao and D. Zhu, *Adv. Mater.*, 2014, **26**, 2862–2867.

44 H. Shen, Y. Zou, Y. Zang, D. Huang, W. Jin, C.-A. Di and D. Zhu, *Mater. Horiz.*, 2018, **5**, 240–247.

45 T. Someya, H. E. Katz, A. Gelperin, A. J. Lovinger and A. Dodabalapur, *Appl. Phys. Lett.*, 2002, **81**, 3079–3081.

46 F. J. Zhang, G. Qu, E. Mohammadi, J. Mei and Y. Diao, *Adv. Funct. Mater.*, 2017, **27**, 1701117.

47 H. Li, Y. Shi, G. Han, J. Liu, J. Zhang, C. Li, J. Liu, Y. Yi, T. Li, X. Gao, C. Di, J. Huang, Y. Che, D. Wang, W. Hu, Y. Liu and L. Jiang, *Angew. Chem., Int. Ed.*, 2020, **59**, 4380–4384.

48 C. Pitsalidis, M. P. Ferro, D. Iandolo, L. Tzounis, S. Inal and R. M. Owens, *Sci. Adv.*, 2018, **4**, eaat4253.

49 S. Inal, A. Hama, M. Ferro, C. Pitsalidis, J. Oziat, D. Iandolo, A.-M. Pappa, M. Hadida, M. Huerta, D. Marchat, P. Mailley and R. M. Owens, *Adv. Biosyst.*, 2017, **1**, 1700052.

50 X. Zhang, B. Wang, L. Huang, W. Huang, Z. Wang, W. Zhu, Y. Chen, Y. Mao, A. Facchetti and T. J. Marks, *Sci. Adv.*, 2020, **6**, eaaz1042.

51 S. Arshavsky-Graham, N. Massad-Ivanir, E. Segal and S. Weiss, *Anal. Chem.*, 2019, **91**, 441–467.

52 M. T. Hwang, I. Park, M. Heiranian, A. Taqieddin, S. You, V. Faramarzi, A. A. Pak, A. M. van der Zande, N. R. Aluru and R. Bashir, *Adv. Mater. Technol.*, 2021, **6**, 2100712.

53 M. T. Hwang, M. Heiranian, Y. Kim, S. You, J. Leem, A. Taqieddin, V. Faramarzi, Y. Jing, I. Park, A. M. van der Zande, S. Nam, N. R. Aluru and R. Bashir, *Nat. Commun.*, 2020, **11**, 1543.

54 L. Huang, Z. Wang, J. Chen, B. Wang, Y. Chen, W. Huang, L. Chi, T. J. Marks and A. Facchetti, *Adv. Mater.*, 2021, **33**, 2007041.

55 L. Li, P. Gao, M. Baumgarten, K. Müllen, N. Lu, H. Fuchs and L. Chi, *Adv. Mater.*, 2013, **25**, 3419–3425.

56 T. Shaymurat, Q. Tang, Y. Tong, L. Dong and Y. Liu, *Adv. Mater.*, 2013, **25**, 2269–2273.

57 S. Mun, Y. Park, Y.-E. K. Lee and M. M. Sung, *Langmuir*, 2017, **33**, 13554–13560.

58 K. Shoorideh and C. O. Chui, *Proc. Natl. Acad. Sci. U. S. A.*, 2014, **111**, 5111–5116.

59 K. S. Park, J. J. Kwok, P. Kafle and Y. Diao, *Chem. Mater.*, 2021, **33**, 469–498.

60 S. Chen, Z. Li, Y. Qiao and Y. Song, *J. Mater. Chem. C*, 2021, **9**, 1126–1149.

61 J. Rivnay, S. C. Mannsfeld, C. E. Miller, A. Salleo and M. F. Toney, *Chem. Rev.*, 2012, **112**, 5488–5519.

62 H. Wang, Y. Xu, X. Yu, R. Xing, J. Liu and Y. Han, *Polymer*, 2013, **5**, 1272–1324.

63 H. Dong, X. Fu, J. Liu, Z. Wang and W. Hu, *Adv. Mater.*, 2013, **25**, 6158–6183.

64 H. Li, J. Song, J. Xiao, L. Wu, H. E. Katz and L. Chen, *Adv. Funct. Mater.*, 2020, **30**, 2004378.

65 H. Takenaka, T. Ogaki, C. Wang, K. Kawabata and K. Takimiya, *Chem. Mater.*, 2019, **31**, 6696–6705.

66 K. Feng, X. Zhang, Z. Wu, Y. Shi, M. Su, K. Yang, Y. Wang, H. Sun, J. Min, Y. Zhang, X. Cheng, H. Y. Woo and X. Guo, *ACS Appl. Mater. Interfaces*, 2019, **11**, 35924–35934.

67 R. K. Hallani, B. D. Paulsen, A. J. Petty, 2nd, R. Sheelamanthula, M. Moser, K. J. Thorley, W. Sohn, R. B. Rashid, A. Savva, S. Moro, J. P. Parker, O. Drury, M. Alsufyani, M. Neophytou, J. Kosco, S. Inal, G. Costantini, J. Rivnay and I. McCulloch, *J. Am. Chem. Soc.*, 2021, **143**, 11007–11018.

68 E. D. Glowacki, M. Irimia-Vladu, S. Bauer and N. S. Sariciftci, *J. Mater. Chem. B*, 2013, **1**, 3742–3753.

69 E. D. Glowacki, G. Voss and N. S. Sariciftci, *Adv. Mater.*, 2013, **25**, 6783–6800.

70 E. D. Glowacki, M. Irimia-Vladu, M. Kaltenbrunner, J. Gsiorowski, M. S. White, U. Monkowius, G. Romanazzi, G. P. Suranna, P. Mastrorilli, T. Sekitani, S. Bauer, T. Someya, L. Torsi and N. S. Sariciftci, *Adv. Mater.*, 2013, **25**, 1563–1569.

71 M. Irimia-Vladu, E. D. Glowacki, P. A. Troshin, G. Schwabegger, L. Leonat, D. K. Susarova, O. Krystal, M. Ullah, Y. Kanbur, M. A. Bodea, V. F. Razumov, H. Sitter, S. Bauer and N. S. Sariciftci, *Adv. Mater.*, 2012, **24**, 375–380.

72 C. Fu, P. J. Beldon and D. F. Perepichka, *Chem. Mater.*, 2017, **29**, 2979–2987.

73 F. J. Zhang, V. Lemaur, W. Choi, P. Kafle, S. Seki, J. Cornil, D. Beljonne and Y. Diao, *Nat. Commun.*, 2019, **10**, 4217.

74 J. Y. Oh, D. Son, T. Katsumata, Y. Lee, Y. Kim, J. Lopez, H. C. Wu, J. Kang, J. Park, X. Gu, J. Mun, N. G. Wang, Y. Yin, W. Cai, Y. Yun, J. B. Tok and Z. Bao, *Sci. Adv.*, 2019, **5**, eaav3097.

75 D. Liu, J. Mun, G. Chen, N. J. Schuster, W. Wang, Y. Zheng, S. Nikzad, J. C. Lai, Y. Wu, D. Zhong, Y. Lin, Y. Lei, Y. Chen, S. Gam, J. W. Chung, Y. Yun, J. B. Tok and Z. Bao, *J. Am. Chem. Soc.*, 2021, **143**, 11679–11689.

76 Y. Zheng, G. J. N. Wang, J. Kang, M. Nikolka, H. C. Wu, H. Tran, S. Zhang, H. Yan, H. Chen, P. Y. Yuen, J. Mun, R. H. Dauskardt, I. McCulloch, J. B. H. Tok, X. Gu and Z. Bao, *Adv. Funct. Mater.*, 2019, **29**, 1905340.

77 T. Higashihara, *Polym. J.*, 2021, **53**, 1061–1071.

78 M. Ashizawa, Y. Zheng, H. Tran and Z. Bao, *Prog. Polym. Sci.*, 2020, **100**, 101181.

79 Z. Ma, D. Kong, L. Pan and Z. Bao, *J. Semicond.*, 2020, **41**, 041601.

80 C. R. Bridges, M. J. Ford, E. M. Thomas, C. Gomez, G. C. Bazan and R. A. Segalman, *Macromolecules*, 2018, **51**, 8597–8604.

81 Y. Wu, Y. Zhao and Y. Liu, *Acc. Chem. Res.*, 2021, **2**, 1047–1058.

82 A. Welford, S. Maniam, E. Gann, X. Jiao, L. Thomsen, S. J. Langford and C. R. McNeill, *Org. Electron.*, 2019, **75**, 105378.

83 B. M. Oh, S. H. Park, J. H. Lee, J. C. Kim, J. B. Lee, H. J. Eun, Y. S. Lee, B. E. Seo, W. Yoon, J. E. Kwon, H. Yun, S. K. Kwak, O. P. Kwon and J. H. Kim, *Adv. Funct. Mater.*, 2021, **31**, 2101981.

84 Z. Wang, Z. Liu, L. Ning, M. Xiao, Y. Yi, Z. Cai, A. Sadhanala, G. Zhang, W. Chen, H. Sirringhaus and D. Zhang, *Chem. Mater.*, 2018, **30**, 3090–3100.

85 J. Yao, C. Yu, Z. Liu, H. Luo, Y. Yang, G. Zhang and D. Zhang, *J. Am. Chem. Soc.*, 2016, **138**, 173–185.

86 S.-F. Yang, X. Zhang, P.-L. Chen, Z.-T. Liu, J.-W. Tian, G.-X. Zhang and D.-Q. Zhang, *Adv. Electron. Mater.*, 2017, **3**, 1700120.

87 Y. Yang, G. Zhang, H. Luo, J. Yao, Z. Liu and D. Zhang, *ACS Appl. Mater. Interfaces*, 2016, **8**, 3635–3643.

88 A. A. Szumska, I. P. Maria, L. Q. Flagg, A. Savva, J. Surgailis, B. D. Paulsen, D. Moia, X. Chen, S. Griggs, J. T. Mefford, R. B. Rashid, A. Marks, S. Inal, D. S. Ginger, A. Giovannitti and J. Nelson, *J. Am. Chem. Soc.*, 2021, **143**, 14795–14805.

89 N. A. Kukhta, A. Marks and C. K. Luscombe, *Chem. Rev.*, 2022, **122**, 4325–4355.

90 A. F. Paterson, A. Savva, S. Wustoni, L. Tsetseris, B. D. Paulsen, H. Faber, A. H. Emwas, X. Chen, G. Nikiforidis, T. C. Hidalgo, M. Moser, I. P. Maria, J. Rivnay, I. McCulloch, T. D. Anthopoulos and S. Inal, *Nat. Commun.*, 2020, **11**, 3004.

91 A. M. Pappa, D. Ohayon, A. Giovannitti, I. P. Maria, A. Savva, I. Uguz, J. Rivnay, I. McCulloch, R. M. Owens and S. Inal, *Sci. Adv.*, 2018, **4**, eaat0911.

92 D. Ohayon, G. Nikiforidis, A. Savva, A. Giugni, S. Wustoni, T. Palanisamy, X. Chen, I. P. Maria, E. Di Fabrizio, P. Costa, I. McCulloch and S. Inal, *Nat. Mater.*, 2020, **19**, 456–463.

93 B. Kang, M. Jang, Y. Chung, H. Kim, S. K. Kwak, J. H. Oh and K. Cho, *Nat. Commun.*, 2014, **5**, 4752.

94 L. Torsi, A. J. Lovinger, B. Crone, T. Someya, A. Dodabalapur, H. E. Katz and A. Gelperin, *J. Phys. Chem. B*, 2002, **106**, 12563–12568.

95 A. J. Smith, C. Wang, D. Guo, C. Sun and J. Huang, *Nat. Commun.*, 2014, **5**, 5517.

96 L. Zhang and T. Andrew, *Adv. Electron. Mater.*, 2018, **4**, 1800271.

97 Y. Yuan, G. Giri, A. L. Ayzner, A. P. Zoombelt, S. C. Mannsfeld, J. Chen, D. Nordlund, M. F. Toney, J. Huang and Z. Bao, *Nat. Commun.*, 2014, **5**, 3005.

98 X. Gu, L. Shaw, K. Gu, M. F. Toney and Z. Bao, *Nat. Commun.*, 2018, **9**, 534.

99 F. Molina-Lopez, H. Yan, X. Gu, Y. Kim, M. F. Toney and Z. Bao, *Adv. Funct. Mater.*, 2017, **27**, 1605503.

100 C. Teixeira da Rocha, G. Qu, X. Yang, R. Shivhare, M. Hambsch, Y. Diao and S. C. B. Mannsfeld, *ACS Appl. Mater. Interfaces*, 2019, **11**, 30079–30088.

101 F. Molina-Lopez, H. C. Wu, G. J. N. Wang, H. Yan, L. Shaw, J. Xu, M. F. Toney and Z. Bao, *Adv. Electron. Mater.*, 2018, **4**, 1800110.

102 Z. Zhang, B. Peng, X. Ji, K. Pei and P. K. L. Chan, *Adv. Funct. Mater.*, 2017, **27**, 1703443.

103 F. Zhang, E. Mohammadi, X. Luo, J. Strzalka, J. Mei and Y. Diao, *Langmuir*, 2018, **34**, 1109–1122.

104 D.-K. Kim, P. Vincent, J. Jang, I. M. Kang, H. Kim, P. Lang, M. Choi and J.-H. Bae, *Appl. Surf. Sci.*, 2020, **504**, 144362.

105 D. H. Kim, H. S. Lee, H.-J. Shin, Y.-S. Bae, K.-H. Lee, S.-W. Kim, D. Choi and J.-Y. Choi, *Soft Matter*, 2013, **9**, 5355–5360.

106 E. Mohammadi, G. Qu, P. Kafle, S.-H. Jung, J.-K. Lee and Y. Diao, *Mol. Syst. Des. Eng.*, 2020, **5**, 125–138.

107 E. Mohammadi, C. Zhao, F. Zhang, G. Qu, S. H. Jung, Q. Zhao, C. M. Evans, J. K. Lee, D. Shukla and Y. Diao, *ACS Appl. Mater. Interfaces*, 2019, **11**, 22561–22574.

108 E. Mohammadi, C. K. Zhao, Y. F. Meng, G. Qu, F. J. Zhang, X. K. Zhao, J. G. Mei, J.-M. Zuo, D. Shukla and Y. Diao, *Nat. Commun.*, 2017, **8**, 16070.

109 E. Mohammadi, P. Kafle, K. Y. Huang, W. Zhu, J. Huang, S. H. Jung, J. K. Lee, C. M. Evans and Y. Diao, *ACS Appl. Mater. Interfaces*, 2020, **12**, 2753–2762.

110 P. Kafle, F. Zhang, N. B. Schorr, K. Y. Huang, J. Rodríguez-López and Y. Diao, *Adv. Funct. Mater.*, 2020, **30**, 1909787.

111 H.-W. Zan, M.-Z. Dai, T.-Y. Hsu, H.-C. Lin, H.-F. Meng and Y.-S. Yang, *IEEE Electron Device Lett.*, 2011, **32**, 1143–1145.

112 G. Rajeev, B. Prieto Simon, L. F. Marsal and N. H. Voelcker, *Adv. Healthcare Mater.*, 2018, **7**, 1700904.

113 X. Guo, L. Liu, Z. Zhuang, X. Chen, M. Ni, Y. Li, Y. Cui, P. Zhan, C. Yuan, H. Ge, Z. Wang and Y. Chen, *Sci. Rep.*, 2015, **5**, 15947.

114 H. Tai, X. Li, Y. Jiang, G. Xie and X. Du, *Sensors*, 2015, **15**, 2086–2103.

115 Q. H. Wang, S. H. Wu, F. Ge, G. B. Zhang, H. B. Lu and L. Z. Qiu, *Adv. Mater. Interfaces*, 2016, **3**, 1600518.

116 I. Jalan, L. Lundin and J. van Stam, *Materials*, 2019, **12**, 3889.

117 S. Wu, G. Wang, Z. Xue, F. Ge, G. Zhang, H. Lu and L. Qiu, *ACS Appl. Mater. Interfaces*, 2017, **9**, 14974–14982.